FEMU based identification of the creep behavior of Zircaloy-4 claddings under simulated RIA thermo-mechanical conditions

T. Jailin, N. Tardif, J. Desquines, P. Chaudet, Michel Coret, Marie-Christine Baietto, V. Georgenthum

FEMU based identification of the creep behavior of Zircaloy-4 claddings under simulated RIA thermo-mechanical conditions.

T. Jailin[a,b], N. Tardif[b,*], J. Desquines[a], P. Chaudet[b], M. Coret[c], M.-C. Baietto[b], V. Georgenthum[a]

[a] *Institut de Radioprotection et de Sûreté Nucléaire (IRSN), PSN-RES, Cadarache, Saint Paul lez Durance, France*
[b] *Univ Lyon, INSA-Lyon, CNRS UMR5259, LaMCoS, F-69621, France*
[c] *École Centrale de Nantes, GeM (UMR 6183), Nantes, France*

Abstract

This study aims to identify the creep behavior of Zircaloy-4 fuel claddings under simulated reactivity initiated accident (RIA) thermo-mechanical conditions. In a previous work ballooning creep tests performed in simulated RIA conditions were described. A challenge to overcome when analyzing these experiments is that ballooning tests imply structural effects during the deformation of the specimen that have to be taken into account to identify the creep behavior of the material. In this paper a FEMU (finite element model updating) based identification is proposed to identify the creep law of the cladding, weakly coupled to the phase transformation of the material at high temperatures. Since the loading conditions are solely known in the part of the optical field of the cameras used for stereocorrelation, only this region is modeled using a Love-Kirchhoff assumption to impose the boundary conditions through the sample thickness. A Norton creep law, whose parameters are expressed as a function of the β phase fraction in the material, is identified and reproduces the first 10 seconds of the experiments with mean errors on the radial displacement rates of about 10%. Finally, an extension to higher time scale is proposed in Norton's law to model the non linearity in the material response by taking into account the grain growth contribution.

Keywords: RIA, Identification, Creep, Zircaloy-4, Full-field measurements, FEMU

1. Introduction

The Reactivity Initiated Accident (RIA) is one of the design basis accidents studied for Pressurized Water Reactors. It results from a sudden insertion of reactivity within the nuclear core. Regarding the fuel rod behavior, it can be split in two consecutive phases: the Pellet Clad Mechanical Interaction (PCMI) phase, followed by the post-Departure from Nucleate Boiling (post-DNB) phase. During this latter phase, the temperature of the fuel claddings may increase up to temperatures greater than 900 °C with very fast heating rates (around 1000 °C/s), meanwhile the claddings are internally pressurized by filling gas and fission gas release [1]. For safety purposes, the least penalizing transients leading to fuel rod failure must be determined, which requires a precise knowledge of the cladding constitutive law in all of these conditions. Identifying a constitutive model of the fuel cladding response in post-DNB conditions is then of great interest.

It is well-known that the thermo-mechanical properties of a material are strongly linked to its microstructure, and that the microstructure depends on the fabrication process. From this, it follows that it is sometimes necessary to work directly on structural samples, in order to take into account the effects of geometry and fabrication process of the specimen on its thermo-mechanical behavior. On another hand, the loading conditions may also play an important role in the material response. As an example, the heating rate may affect the phase transformation of the material [2, 3, 4] and thus may affect its mechanical properties [3, 5, 6]. Therefore, the identification of a constitutive model must be done in conditions as close as possible to real life conditions in order to avoid extrapolations that may lead to uncontrolled discrepancies. Following this idea, an innovative device was developed recently in [6] to reproduce simulated post-DNB thermo-mechanical conditions directly on cladding sections made of Zircaloy-4. It is worth noting that the effects of irradiation-induced defects were not considered in this work. Such effects are very complicated to study, especially for safety reasons. Even if irradiation defects tend to recover at high temperatures [7, 8], nothing indicates that this recovery is fast enough to have no impact during the post-DNB phase of a RIA. Further studies should be carried out to investigate the influence of irradiation defects after high thermal transients.

In [6], creep ballooning tests were performed on fuel cladding sections under conditions representative of the post-DNB phase of a RIA: the tubular sample was first internally pressurized, followed by heating until high temperature with fast heating rate ($\simeq$ 1200 °C/s). The temperatures of interest ranged from 840 to 1020 °C. The ballooning deformation and the temperature at the sample surface were measured by stereo-correlation and near infrared thermography, respectively. The sample, made of Zircaloy-4 alloy, shows a ($\alpha \rightarrow \beta$) phase transformation at high temperature from around 800 to 1000 °C [3, 9, 10, 4]. This transformation, studied and modeled in [4]

*Corresponding author
Email address: author@insa-lyon.fr (N. Tardif)

from equilibrium to 2000 °C/s, shows a strong dependence to the heating rate. The creep results of [6] evidenced a close link between the phase transformation and the mechanical properties, as well as an important impact of the heating rate on the mechanical properties of the material. However, due to structural effect the stress state could not be accurately estimated to identify with sufficient accuracy a constitutive creep law.

To the authors knowledge no constitutive model has yet been identified in post-DNB conditions, *i.e.* with very fast heating rate, mainly due to experimental and identification difficulties. Based on the finite element model updating (FEMU) method [11, 12, 13, 14] this paper aims to identify a creep law weakly coupled to the phase transformation, using the experimental results of [4, 6]. A single and continuous law is developed to reproduce the experimental creep results obtained in simulated post-DNB conditions from 840 to 1020 °C. The impact of the heating rate on the creep properties is also discussed using existing results from the literature. The present work also details a procedure to model the experiments, since the loading conditions were only known in a restricted region of the samples during the tests. The 3D-modeling, based on a Love-Kirchhoff assumption through the thickness, is presented as well as its sensitivity to input parameters to ensure the efficiency of the identification algorithm.

This paper is decomposed as follows. First, the experimental results, the modeling of the experiments and the FEMU method are presented. The identification procedure is then validated on a virtual test case representative of the experiments. In the fourth part a creep law coupled to the phase transformation is identified based on the experimental results of [6]. Finally, an extension to higher time scale is proposed in Norton's law by taking into account the grain size contribution to model the non linearity in the material response.

2. Experimental results, material and methods

2.1. Experimental device, specimens and results

The so-called ELLIE test facility and the experimental results are here briefly summarized. More information can be found in [6] and [15].

The specimens are 90 mm long fuel cladding sections made of stress relieved annealed Zircaloy-4. The tubes have an external diameter of 9.5 mm and a wall-thickness of 0.57 mm. The samples are loaded on the ELLIE device, which enables reproducing simulated post-DNB conditions. The experimental procedure can be described as follow : (i) the samples are mechanically loaded with an internal pressure and a compressive force, (ii) when the mechanical loading is stabilized the samples are heated using an induction system until a regulation temperature with a heating rate of around 1200 °C/s, (iii) the thermal and the mechanical loads are maintained to observe the creep deformation of the sample. Around twenty tests were performed in these simulated RIA conditions with temperatures of interest ranging from 840 to 1020 °C and with two relative levels of pressure of 7 and 11 bar. One additional experiment was carried out with a pressure of 9 bar to validation purposes, as presented in the following. All the experiments were performed within an enclosure where an argon flush was set up during the tests to prevent the samples from oxidation.

Figure 1 presents how the experimental results were extracted from the tests. The thermal and the kinematics full-fields were measured by near infrared (NIR) thermography and stereo-correlation (3D-DIC), respectively. A methodology, presented in [16], enabled the two kinds of fields to be obtained using the same two CMOS cameras. Thus, the displacement evolution, as well as the temperature evolution, were obtained on the whole region seen by the cameras. Using these data, the mean creep rates were computed as a function of the mean temperature at each node of the correlation mesh and for each test during the first ten seconds of the experiments, which is the approximate maximum duration of the boiling crisis of a RIA. Gathering the results of all the tests in one single graph, a complex creep behavior has been evidenced.

Three different creep domains have been identified from 840 to 1020 °C. The first one ranged from 840 to 910 °C. In this domain, the β fraction is low ($\leqslant 10\%$), the grains are small and equiaxed, and the creep rate increases with the temperature. In the second domain, defined from 910 to 970 °C, the creep rate decreases while the temperature increases. The grain size remains small and the β fraction ranged from around 10 to 100%. Because the temperature was maximal at the middle of the sample and decreased toward the jaws, two areas affected by higher creep deformation than elsewhere were obtained on the specimens located from either side of the hottest region. It resulted in the so called "butternut shape" profile on the samples at the end of the experiments. The third domains corresponds to the pure β domain at 970 °C. In this domain the creep rate increases anew with the temperature. As the β grain growth is not blocked anymore by the remaining α phase, big β grains are observed in this domain. In [6], a uniform stress in the two phases was assumed to estimate the creep behavior of the material in the two-phase domain. However, due to structural effects that may take place within the samples during the experiments, the stress state could not be accurately estimated, at least with enough confidence to identify a constitutive law.

2.2. Material behavior

Phase transformation

Zircaloy-4 presents a hexagonal close-packed α phase stable under around 800 °C, and a body centered cubic β phase stable above around 1000 °C. Between these two temperatures, the two phases coexist within the material. The phase transformation of the material is computed using the model characterized in [4], which is based on a Leblond's equation [17]. It reads:

$$\frac{df_\beta}{dt} = \begin{cases} \dfrac{f_{eq}(T) - f_\beta}{\tau(T)} & \text{if } f_\beta > F_{500}(T) \\ \dfrac{F_{500}(T) - f_\beta}{dt} & \text{otherwise.} \end{cases} \quad (1)$$

where T is the temperature, f_β is the fraction of β, $f_{eq}(T)$ is the fraction of β at equilibrium for a temperature T, $F_{500}(T)$ is a saturation function describing the fraction of β at a temperature T

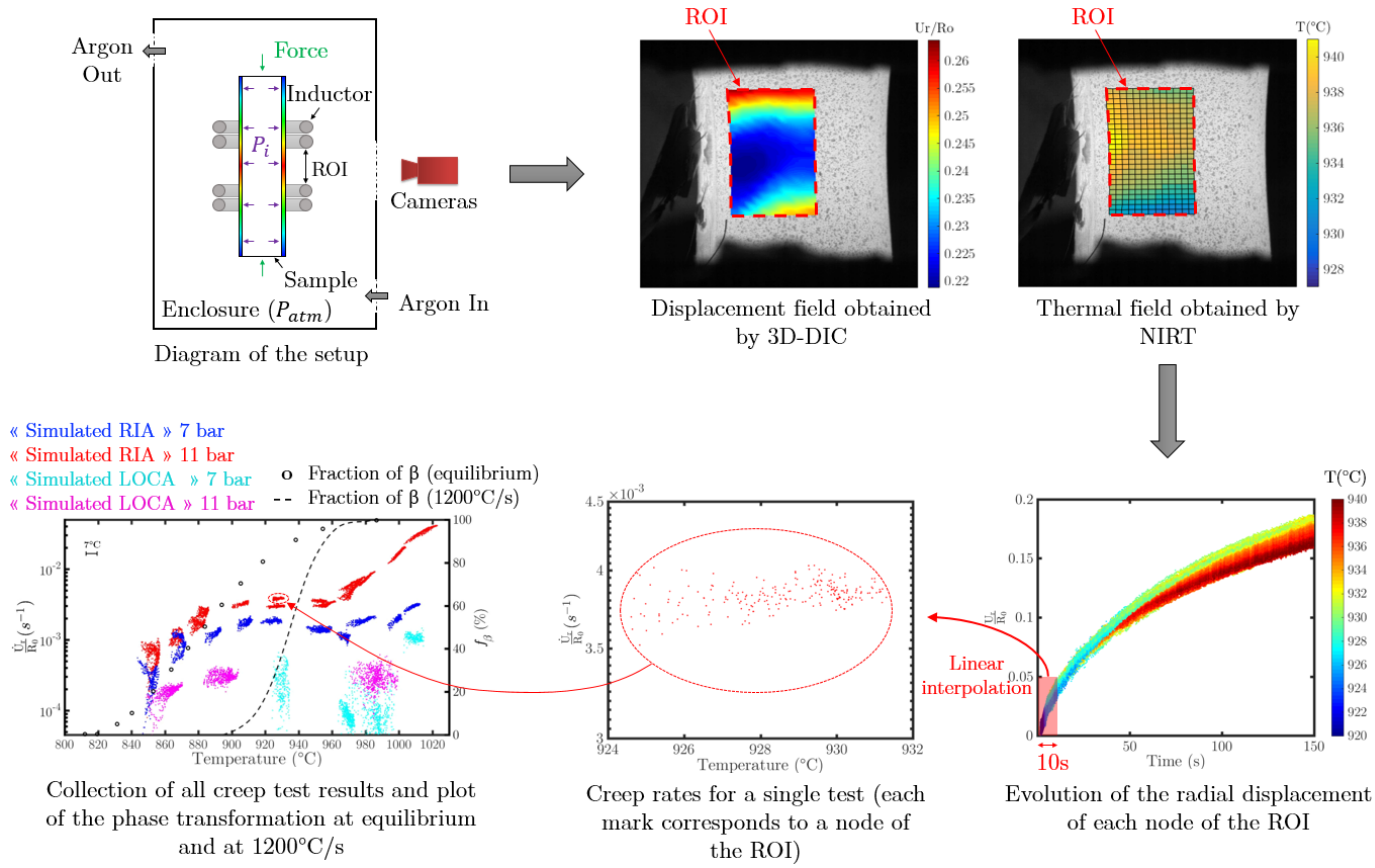

Figure 1: Procedure used in [6] to extract the experimental results from the creep tests.

during a heating where the heating rate is greater than 500 °C/s, and $\tau(T)$ represents the characteristic time of transformation.

$\tau(T)$ is defined using an Arrhenius-type equation such as:

$$\tau(T) = \left[k_0.e^{-\frac{Q_f}{R.T}}\right]^{-1}, \quad (2)$$

where k_0 is a kinetic prefactor, Q_f is an activation energy and R is the perfect gas constant.

The equilibrium function f_{eq} reads:

$$f_{eq}(T) = 1 - e^{-[C.(T-T_0)]^n}, \quad (3)$$

where C, T_0 and n are three material constants characterizing the rate of transformation during heat up phase.

The function F_{500} is defined using the same formulation:

$$F_{500}(T) = 1 - e^{-[C_2.(T-T_2)]^{n_2}}, \quad (4)$$

where C_2, T_2 and n_2 are three constants describing the fastest transformation rate observed in the material. Above 500 °C/s heating rate has no more influence on the phase transformation kinetics.

The values of the parameters of Equations (2), (3) and (4) are given in Table 1.

$\tau(T)$	$\ln(k_0)$	79.62
	Q_f (kJ.mol^{-1})	764.2
$f_{eq}(T)$	C (°C^{-1})	6.89 10^{-3}
	T_0 (°C)	750.0
	n	4.14
$F_{500}(T)$	C_2 (°C^{-1})	1.36.10^{-2}
	T_2 (°C)	865.4
	n_2	4.18

Table 1: Parameters of Equations (2), (3) and (4).

Mechanical behavior

Since the deformation levels reached during the tests can be important, true stress and strain definitions are used in this study. The total deformation of the material can be decomposed such as:

$$\underline{\underline{\varepsilon}} = \underline{\underline{\varepsilon}}^e + \underline{\underline{\varepsilon}}^{th} + \underline{\underline{\varepsilon}}^{vp}, \quad (5)$$

where $\underline{\underline{\varepsilon}}$, $\underline{\underline{\varepsilon}}^e$, $\underline{\underline{\varepsilon}}^{th}$, and $\underline{\underline{\varepsilon}}^{vp}$ are the total, elastic, thermal and visco-plastic deformations, respectively.

The elastic behavior is described using a isotropic description with a temperature-dependent Young's Modulus E described in Equation (6) and a Poisson's ratio of 0.342 [18].

$$E(T) = 116.1 - 59.10^{-3}.(T + 273.15) \text{ [GPa]}, \quad (6)$$

where the temperature T is expressed in °C.

The isotropic thermal deformation is described using a coefficient of thermal expansion (CTE) associated to each phase. The CTE of the α and β phase are set equal to $9.6.10^{-6}$ °C^{-1} and $1.32.10^{-5}$ °C^{-1}, respectively, according to [4]. The reference temperature at which the thermal strain is considered to be zero is set in each test to be the temperature obtained from the first image of the test by near infrared thermography.

Based on [19], the visco-plastic strain rate tensor $\underline{\underline{\dot{\varepsilon}}}^{vp}$ is defined such as:

$$\underline{\underline{\dot{\varepsilon}}}^{vp} = \frac{3}{2}\,\dot{p}\,\frac{\underline{\underline{\sigma}}'}{\sigma_{vM}}, \tag{7}$$

where σ_{vM} is the von Mises stress, $\underline{\underline{\sigma}}'$ is the deviatoric stress tensor and $\dot{p}$ is the accumulated plastic strain rate, referred for convenience as the creep rate hereinafter.

The creep rate $\dot{p}_i$ of each phase i is defined using a Norton's formulation commonly used to describe the steady stage of creep in zirconium alloys [20, 21, 22, 23], which reads:

$$\dot{p}_i = A_i\,\sigma_{vM}^{n_i}\exp\left(-\frac{Q_i}{RT}\right), \quad i=\alpha;\beta \tag{8}$$

where A_i is a constant, n_i is the Norton's exponent, Q_i is an activation energy.

The material behavior in the two-phase domain is modeled assuming a serial distribution of the two phases [6, 24], which can be formulated such as:

$$\underline{\underline{\Sigma}} = \underline{\underline{\sigma_\alpha}} = \underline{\underline{\sigma_\beta}} \tag{9}$$

$$\dot{\bar{p}} = \dot{p}_\alpha.(1-f_\beta) + \dot{p}_\beta.f_\beta \tag{10}$$

where Σ, σ_α and σ_β are the homogenized stress, the stress in the α phase and the stress in the β phase, respectively. f_β is the β phase fraction, $\dot{\bar{p}}$, $\dot{p}_\alpha$ and $\dot{p}_\beta$ are the homogenized accumulated plastic strain rate, the accumulated plastic strain rate in the α phase and the accumulated plastic strain rate in the β phase, respectively.

It follows that 6 parameters $\{A_i\,;\,n_i\,;\,Q_i\}$ have to be identified in the domains $i=\{\alpha;\beta\}$.

It is worth precising that three assumptions were used to model the material behavior in this study. (i) It is assumed that the stress state does not influence the phase transformation. Phase transformation studies under loading should be carried out to validate this assumption. (ii) Because of the very fast recrystallisation at high temperature [25], an isotropic behavior was considered. Anisotropy could be taken into account for lower temperatures, using a Hill definition of the equivalent stress for instance. (iii) The behavior of the α and β phase are considered to follow the same law in the single and two-phase domain while their microstructure and chemical composition may be different.

2.3. The FEMU method

The identification problem is solved using the FEMU method, which consists in comparing experimental to finite element (FE) results in order to identify a set of parameters λ. A finite element modeling is developed to numerically reproduce the experiments, and of course a constitutive law where the set of parameters λ is sought. The method also requires the definition of a cost-function, which is commonly described using a mean-square formulation on the displacements as follow:

$$\eta^2(\lambda) = \frac{1}{N.\gamma^2}(U_{exp}-U_{num}(\lambda))^t.(U_{exp}-U_{num}(\lambda)), \tag{11}$$

where U_{exp} gathers the experimental radial displacements measured by stereo-correlation, $U_{num}(\lambda)$ gathers the numerical radial displacements obtained with the set of parameters λ, N denotes the number of data extracted from DIC and γ is the standard deviation of noise on the measured displacements. This cost function is expected to be equal to unity if the errors are solely due to noise [13]. Using the 3 directions of the displacements in the cost function didn't induce any differences in the results since the hoop and axial displacements are much less sensitive than the radial ones to ballooning deformations.

The minimization of this cost-function can be resolved by an iterative Gauss-Newton algorithm such as:

$$\delta\lambda = H^{-1}J^t(U_{exp}-U_{num}(\lambda)), \tag{12}$$

where $\delta\lambda$, is the parameter increment, J is the Jacobian matrix gathering the sensitivity fields ($\delta U_{num} = J\delta\lambda$) and H is the approximated Hessian computed such as $H = J^tJ$.

The optimization is considered as converged when the cost-function evolution and the parameter evolution become lower than 1% for an iteration. The sensitivity of the model to the parameters is naturally computed during the minimization process. It is a useful tool to ensure the relevance of the experiments performed to the constitutive model identification. This will be developed in the following.

2.4. Finite element modeling

The thermal loading was not axisymmetric during the experiments. The temperature and the displacements are only known in the region of interest (ROI) at the external surface of the sample. It follows that only this ROI was modeled to numerically duplicate the experiments. The DIC surface mesh is "extruded" toward the radial direction to obtain a 3D mesh as shown in Figure 2. Two elements at the boundary of the correlation mesh are not extruded, in order to limit boundary errors and compute accurately the surface normal. For all the tests, the FE mesh of the ROI represents a section of about 40° of arc length and 9 mm in height. The commercial software Abaqus is used to perform the FE analysis and to account for the geometric non-linearity. Six incompatible mode eight-node brick "C3D8I" elements [26] are used through the thickness to obtain a converged mesh.

The temperature obtained at the surface of the samples by NIR thermography is imposed at each time step to the FE nodes. The induction heating system led to a uniform temperature

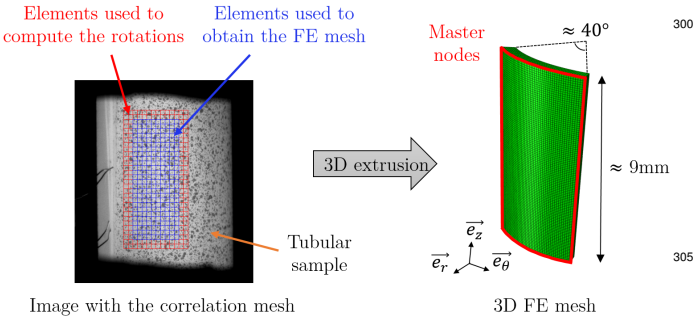

Figure 2: Extrusion of the FE mesh from the correlation mesh.

across the thickness so the temperature imposed at the surface is propagated through the sample thickness. The internal pressure measured during the test is applied on the internal surface of the tube. The outer pressure during the tests being the atmospheric one, the external surface of the cladding is then considered as a free edge. The radial, hoop and axial displacements (U_r ; U_θ and U_z, respectively) measured by 3D-DIC are applied to the master nodes depicted in red in Figures 2 and 3. These master nodes correspond to the nodes of the external surface at the ROI boundaries. It is obvious that the external section cannot neither be let free nor be constrained by propagating the displacements through the thickness, like done for the temperature. To overcome this, a Love-Kirchhoff kinematic is imposed to the external section of the ROI. The slave nodes, depicted in blue in Figure 3 are constrained to have displacement components remaining parallel to the surface normal, while keeping their degree of freedom along this normal. The normal $\vec{n}$ is computed at each time step using the sample topology obtained by stereo-correlation as presented in Figure 3.b.

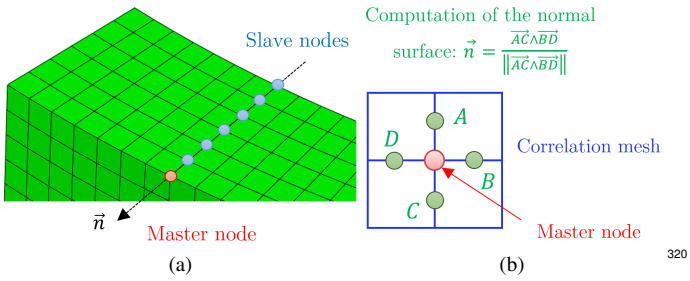

Figure 3: (a) U_r, U_θ and U_z are imposed to the master nodes, the slave nodes are constrained to stay on the normal $\vec{n}$; (b) computation of the normal $\vec{n}$ using the correlation nodes.

The displacements obtained by 3D-DIC were noisy, with noise of around 1 μm for the in-plane displacements and about 5 μm for the out-of plane displacements. To avoid stress concentration and convergence problems the displacements at the edge of the ROI are first smoothed using polynomial functions such as:

$$H(\theta, z) = \sum_{i=0}^{5} \sum_{k=0}^{i} \left(\Xi_{(i-k)k} . \theta^{i-k} . z^{k} \right) \quad (13)$$

where θ and z are the angular and axial coordinates of the nodes, respectively. Ξ_{ij} are the polynomial coefficients.

3. Virtual test: performance evaluation

3.1. Description of the virtual case

To validate the identification method a virtual test case is setup. Five calculations are performed where the tubular sample is entirely modeled (cf. Figure 4). 6 "C3D8I" elements are used through the tube thickness. The axial temperature is imposed using a quadratic function knowing that the temperature is maximal at the center and minimal at the jaws where it is set to 500 °C. A circumferential thermal gradient of 25 °C is imposed to better represent the experiments. The sample is then internally pressurized.

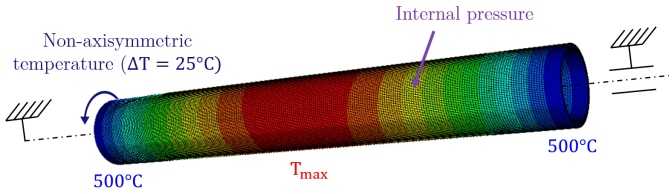

Figure 4: FE modeling of the virtual case.

The visco-plastic behavior of the material is modeled using the Norton's law described in Equation (8). The parameters are set such as $\ln(A) = 11$, $n = 4$ and $Q = 250$ kJ.mol^{-1}. These 3 parameters composed the reference set λ_{ref}.

Five simulations are carried out with different loading conditions as presented in Table 2. The computations are interrupted at a test time of 10 seconds, being the characteristic time of a reactivity initiated accident.

	Test 1	**Test 2**	**Test 3**	**Test 4**	**Test 5**
T_{max} (°C)	950	950	900	930	1000
P_i (bar)	7	11	11	11	7

Table 2: Loading conditions of the virtual case. T_{max} corresponds to the maximal temperature at the center of the sample and P_i correspond to the internal pressure.

The displacements and the temperature are extracted from a region of 40° of arc length and 9 mm in height at the center of the sample to simulate the experimental results U_{exp}. To be representative of the experiments, white noise of 1 μm and 5 μm is added on the in-plane and out-of-plane displacements, respectively, to challenge the convergence stability of the algorithm. The ROI is then modeled following the procedure described in section 2.4. The set of initializing parameters of the creep law is finally strongly perturbed leading to the set λ_0 with $\ln(A)$= 4, $n = 1.5$ and $Q = 120$ kJ.mol^{-1}.

3.2. Sensitivity of the method

Since all the external boundaries of the ROI are fully constrained, one may ask if the calculations are sensitive to a parameter perturbation. To study the sensitivity, the mean sensitivity of a node S_{mean} is defined such as:

$$S_{mean} = \frac{1}{3}\sum_{i=1}^{3}\left|\frac{U_{num}(\lambda) - U_{num}(\lambda+\delta\lambda_i)}{U_{num}(\lambda)}\right|, \qquad (14)$$

where $\lambda = \{A, n, Q\}$ and $\delta\lambda_i$ is a small perturbation applied to the parameter i. $U_{num}(\lambda)$ gathers the numerical radial displacements obtained with the set of parameters λ.

It is then possible to obtain the spatial distribution of sensitivity as well as its temporal evolution at a given node. Examples of sensitivity results are given in Figure 5 for the Test 4 and for a parameter perturbation of 0.2%.

The sensitivity of the test is important with a maximal value of around 0.8% at $t = 10$s at the center of the ROI. The sensitivity at the boundaries is null, because all the degree of freedom are constrained, and increases toward the center. Having an important sensitivity is important to minimize the number of iterations needed and limit the risk of finding a local minimum.

3.3. Results of the virtual test case

The FEMU method is applied using the set λ_0 to initialize the algorithm. The results are given in Figure 6.

The three parameters are found at 95% of the reference parameters at the fifth iteration and at 99% at the eighth iteration. From the eighth iteration the residual evolution and the parameter evolution become lower than 0.5%, the algorithm is then considered as converged. The final residual is equal to 1.09. The mean error on the radial displacement is around 0.5% and the parameters are found with maximal errors of 0.8% compared to their reference values (cf. Table 3).

	Converged parameters	**Relative error**
$\ln(A)$	10.91	0.8%
n	3.98	0.6%
Q (kJ.mol^{-1})	248.9	0.4%
Residual $\eta(\lambda)$	1.09	

Table 3: Converged parameters and relative errors compared to the reference set λ_{ref}.

The virtual test case shows excellent robustness of the identification algorithm and fast convergence. Only 8 iterations are needed to obtain the parameters at 99% of their reference values, while they were initially strongly perturbed. Furthermore, this test case enables validating both the use of a Love-Kirchhoff kinematic across the external section and the smoothing of the displacements at the boundaries of the extracted mesh by polynomial surfaces.

4. Application to the experiments

The method is then applied to the experiments performed in the ELLIE bench simulating post-DNB conditions presented in [6].

4.1. Initialization of the algorithm

The identification process needs $(N_e \times (N_\lambda + 1))$ calculations per iterations, where N_e is the number of experiments modeled and N_λ is the number of sought parameters. To have a maximum test conditions, the 24 experiments of [6] are used in the identification process. It leads to a number of 168 calculations per iterations. In order to minimize the number of iterations it is useful to find the best initial set of parameters λ_0. To do so, two assumptions are formulated to be able to resolve analytically the mechanical problem. First, the stress state during the tests is approximated assuming that the sample can be represented as an open thin-walled cylinder (since a force was applied during the tests to compensate the end caps effect). follows:

$$\sigma_{vM} = \frac{P_i.(R_i + U_r)}{e.(1+\varepsilon_{rr})}, \qquad (15)$$

where P_i is the internal pressure, R_i is the initial inner radius, U_r is the radial displacement, e is the initial thickness and ε_{rr} is the radial deformation obtained using the displacements measured by 3D-DIC and the assumption of volume conservation in the plastic domain.

Second, using the radial displacement measured by stereo-correlation, the strain rate $\dot{\bar{p}}$ is approximated such as:

$$\dot{\bar{p}} = \frac{\dot{U}_r}{R_e(t)}, \qquad (16)$$

where $\dot{U}_r$ is the radial displacement rate, and R_e is the external radius of the sample.

The set of parameters λ_0 is then identified using the Equations (1), (10), (15) and (16). All the radial displacement values obtained in the tests are used to perform the initialization. As a reminder, only the first ten seconds of the tests are studied for the moment.

4.2. Results of the identification

The final values of the parameters obtained after the FEMU procedure are given in Table 4. The residual evolution is presented in Figure 7. The algorithm converged after only 4 iterations. The parameters do not evolve significantly while the residual decreases by 27%. It denotes a high sensitivity of the tests to a parameter perturbation. The final residual is equal to 2.22 times the noise level.

A new scalar is introduced to quantify the error between the model and the experiments: ξ. It represents the mean error on the radial displacement rates of a test, which reads:

$$\xi(\%) = \frac{1}{N}\sum_{i=1}^{N}\left|\frac{\dot{U}_r^{\exp} - \dot{U}_r^{\text{num}}}{\dot{U}_r^{\exp}}\right| \times 100, \qquad (17)$$

where N is the number of nodes on the correlation mesh of a test, $\dot{U}_r^{\exp}$ gathers the radial displacement rates of the test and $\dot{U}_r^{\text{num}}$ gathers the radial displacement rates obtained by calculations with the set λ_f.

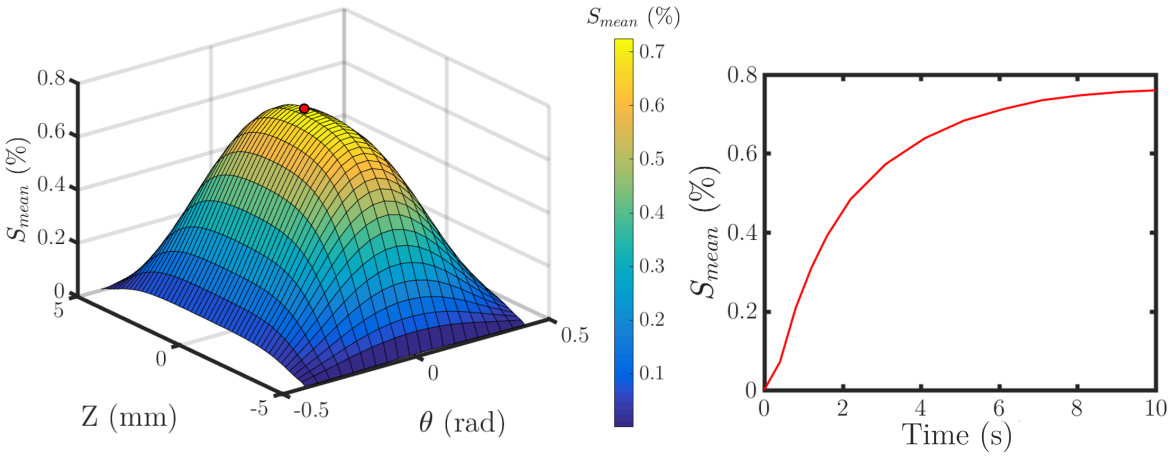

(a) (b)

Figure 5: (a) Sensitivity surface extracted at $t = 10$s for the Test 4 ; (b) temporal evolution of the sensitivity at the center of the ROI (red point in Figure (a)).

	$\ln(A_\alpha)$	n_α	Q_α (kJ.mol^{-1})	$\ln(A_\beta)$	n_β	Q_β (kJ.mol^{-1})
λ_0	48.7	1.11	544.2	43.4	4.53	603.9
λ_f	48.6	1.11	545.0	43.2	4.45	607.6

Table 4: Values of the initial and final set of parameters.

Figure 8 compares the experimental radial displacement rates to the computed ones. The mean approximated strain rate during the first 10 seconds is plotted as a function of the temperature for all the tests and at each node of the correlation mesh. The mean error of each test, described by the Equation (17), is also given in the upper graph. The evolution of the phase fraction is also given at equilibrium and for a heating rate representative of the experiments ($\simeq$ 1200 °C/s), computed using Equation (1). The calculations reproduce the experimental results with good agreements. The mean error ξ on the radial displacement rates is equal to 10.5%, which is considered as very good for these kinds of experiments. The error is more important at the lower temperatures, where the signal/noise ratio is low. A slightly more important error is observed around 970 °C, when the material switches from the two-phase domain to the β domain. A high sensitivity of the metallurgical state to the temperature is expected around this transition [4, 6].

4.3. Validation on an additional experiment

Once identified, the model is validated using an additional experiment, which was not used during the identification process. The internal pressure during the test was 9 bar and the loading conditions are given in Table 5. The results of the calculation are presented in Figure 8.

The residual for this test is 2.47 and the mean error ξ is 10.7%. It corresponds to the mean value obtained for all the tests modeled. Figure 9 presents the displacements and the fraction of β extracted from an axial line at the center of the ROI at $t = 10$s. The temperature distribution is also given. First, it is worth noticing that two more deformed areas are present and are not located at the hottest point which is at the middle. In this domain of temperature, the creep rate decreases while the temperature increases, leading to the "butternut shape" profile on the sample already mentioned in Section 2 (it is the second domain of creep identified in [6]). Higher strains are observed at lower temperatures, where the β fraction is lower. It can be observed that this "butternut shape" profile is well reproduced by the model. The mean error on the displacements between the calculation and the experiment is 4.8%. The model is thus considered as valid within the range of loading conditions investigated.

T_{ROI} (°C)	dT/dt (°C/s)	OS^+ (°C)	ΔT (°C)
948	1281	5	941 - 952

Table 5: Experimental conditions of the additionally experiment performed. The internal pressure was 9 bar. T_{ROI} represents the temperature computed at the center of the ROI by NIR thermography. dT/dt is the mean value of the thermal transient measured by the pyrometer. OS^+ is the difference between the maximal temperature reaches at the end of the transient and the regulation temperature [6]. ΔT gives the mean thermal distribution within the ROI at $t = 10$s.

4.4. Discussion

This work succeeded in reproducing the creep response of Zircaloy-4 in the whole domain of loading conditions investigated in [6] using a single and continuous equation. However some points and assumptions need to be discussed.

A Norton's creep law is used to model the creep behavior of the two phases while the steady stage of creep is not reached yet. However, as the test duration analyzed is short (10 seconds) and as the level of deformation remains low at 10 seconds the

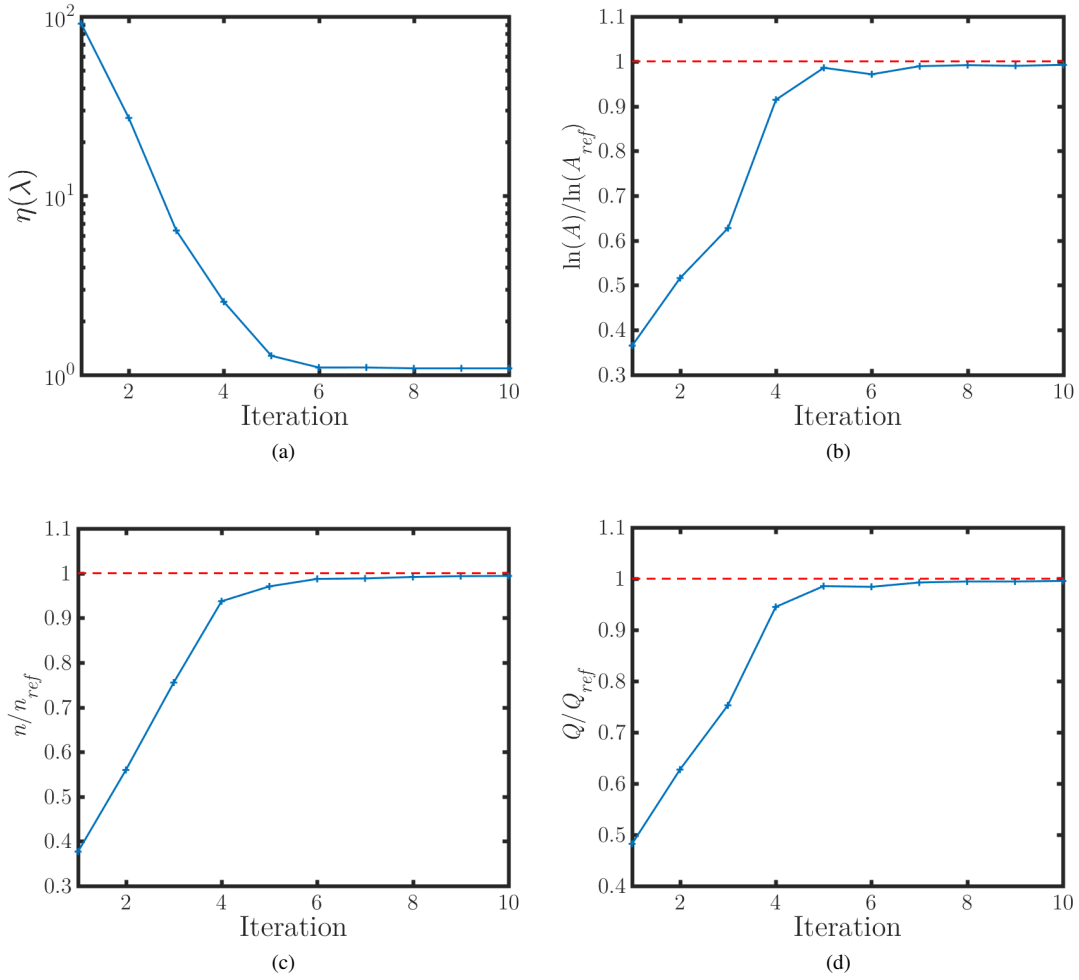

Figure 6: Results of the virtual case: (a) evolution of the residual η ; (b) evolution of $\ln(A)/\ln(A_{\text{ref}})$; (c) evolution of n/n_{ref} ; (d) evolution of Q/Q_{ref}.

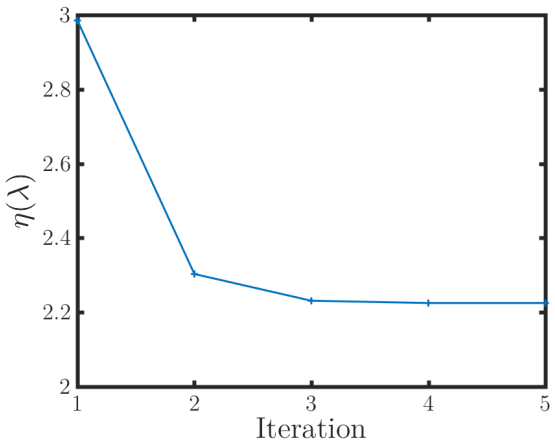

Figure 7: Evolution of the residual η for the identification of a creep law reproducing the first ten seconds of all the experiments performed in simulated post-DNB conditions (serial assumption).

model is able to reproduce the experimental data. The next section proposes an extension of the model at higher time scale by taking into account the grain growth contribution in the creep response of the material.

The assumption was made that the phases are present in a serial distribution in the two phase domain. It led to good results, and succeeded to reproduce the "butternut" profile on the sample in the two-phase domain. However additional data in the pure α domain at equilibrium, *i.e.* at lower temperatures, are still needed to validate this serial assumption.

A stress exponent around unity is identified for the α phase, which is characteristic of a diffusion creep mechanism. On the other hand, a dislocation creep mechanism is observed in the β phase, evidenced by a stress exponent of around 4.5. These observations are in good agreement with the literature for this low level of applied stress [21, 20, 27]. Since the results of the literature were obtained in isothermal conditions with low heating rate, it may be concluded that there is no impact of the heating rate on the activated creep mechanism up to 1200 °C/s. It is also worth noticing that in [6, 4] a small grain size was evidenced in the α phase, and much bigger grains were observed in the pure

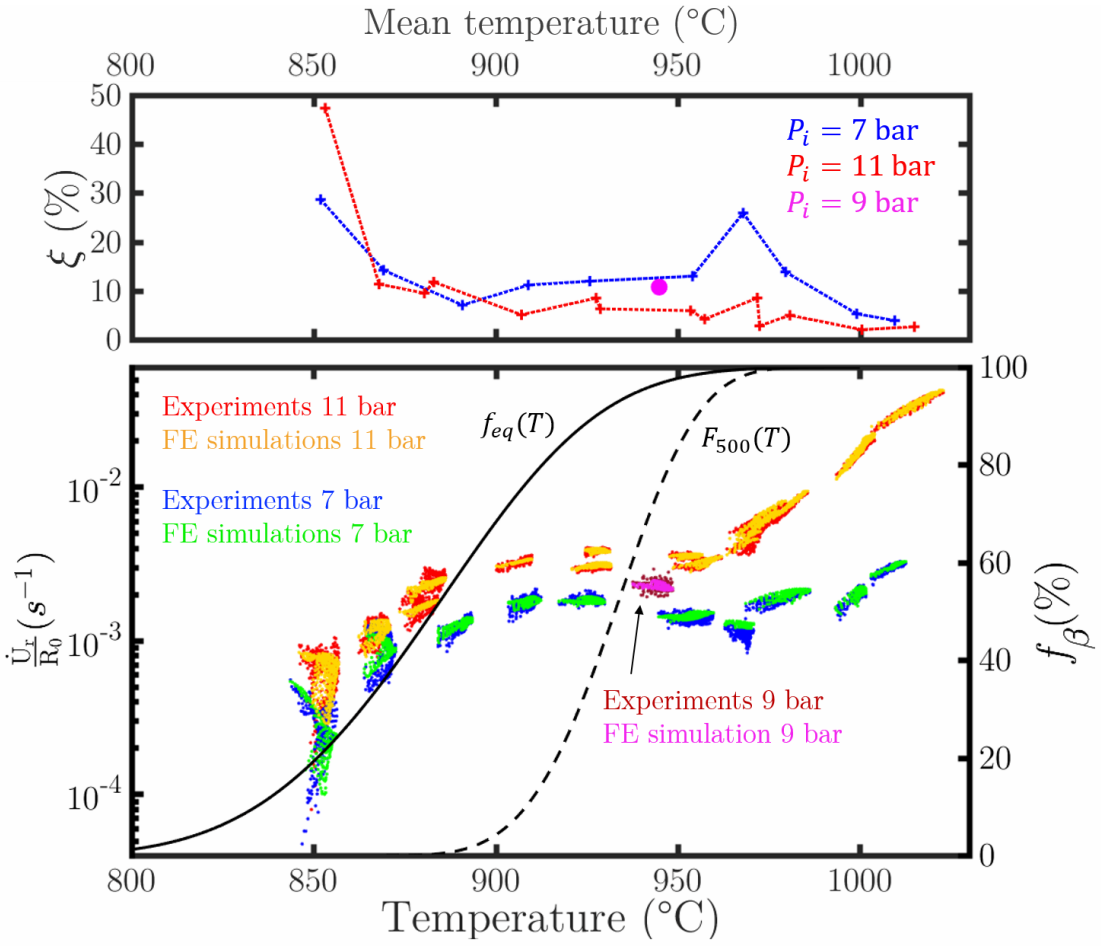

Figure 8: Comparison between the numerical creep rates, computed using the final set of parameters λ_f and the equations given in Section 2 (serial assumption), and the experimental results of [6]. The evolution of the phase fraction against temperature is also given at equilibrium and under a heating rate of 1200 °C/s.

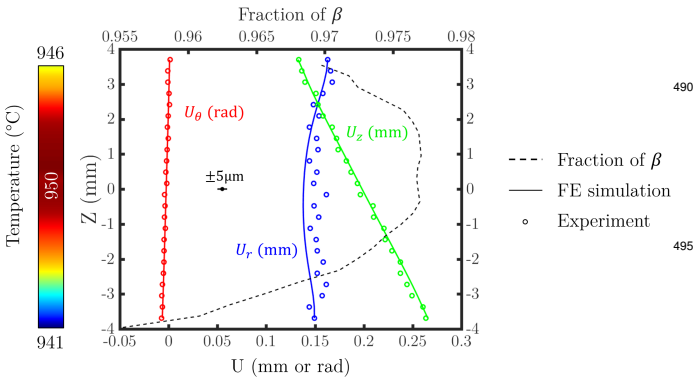

Figure 9: Comparison between the experimental and the numerical displacements obtained along an axial line at the middle of the ROI for the 9 bar test.

β phase. These grain sizes are consistent with the creep mechanisms identified in each phase since diffusion and dislocation creeps are usually favored by small and important grain sizes, respectively.

While the stress exponents identified are in the expected order of magnitude under the tested conditions, the activation energies identified following a very fast heating are much higher in the two phases than the ones identified in the literature in isothermal conditions. The activation energy in the α phase for a diffusion mechanism is usually estimated around 150kJ/mol [27, 21, 20] for isothermal tests, and the one in the β phase for a dislocation mechanism is about 140kJ/mol [28, 29, 30, 21]. Activation energies of about 600kJ/mol were identified in the two phases when the material was heated with a very fast heating rate. Additional microstructure analysis should be carried out to better understand the underlying mechanisms behind this change in the activation energies. It is also possible that the activation energy accommodates in the minimization process to fit the experimental data, because of the assumptions made to model the material behavior (i.e. a serial distribution of the two phases, no impact of the stress state on the phase transformation, and no change in the creep law in the α and β phases between the single and two-phase domains). More experimen-

tal data (especially results in the pure alpha domain) is needed to discriminate whether these energy values are true or come from one (or several) of the bias(es) mentioned above.

From a numerical point of view one may notice that the residual obtained with the initial set of parameters is close to the converged residual. It has been demonstrated that this is not due to a low sensitivity of the calculations to the parameter values. The low evolution of the residual can be explained by the high quality of the initialization, which was carried out with a large amount of data, and with assumptions that appear to be not far from the truth. In some case it may be useful to spend some time in finding a good starting set, in order to save an important calculation time afterwards and possibly avoid diverging problems.

In [6] only the first ten seconds of the experiments were analyzed since it is the characteristic time of a reactivity initiated accident. The relatively small strain levels reached at 10 seconds enables the Norton's law to reproduce well the experimental data, but it cannot be extended to longer test times. The following section proposed to extend the identification up to the first 100 seconds of eight tests located in the two-phase domain. In order to take into account the secondary stage of creep the impact of the grain size evolution on the creep properties is modeled. Furthermore, since the deformations are higher at 100 s the structural effects have to be taken into account with a finite element based identification method, which enables reproducing the 3D stress state in the material.

4.5. Extension to 100s

In order to be more representative of other accidents, like the loss of coolant accident, the identification procedure was also performed on eight experiments carried out in the two-phase domain during the first 100 seconds of the tests.

The primary stage of creep is taken into account by adding the grain size evolution in the Norton's creep law [31, 22]. The creep rate now reads :

$$\dot{E} = \sum_i A_i \left(\frac{D_{0i}}{D_i}\right)^{g_i} \sigma_{vM}^{n_i} \exp\left(-\frac{Q_i}{RT}\right) f_i, \qquad \text{with } i = \{\alpha;\beta\}, \tag{18}$$

where the subscript i defined the phase, D_{0i} is the initial grain size of the phase i, D_i is the grain size of the phase i.

The grain size evolution is modeled using the following equation [22, 32] :

$$\frac{dD_i}{dt} = K_i \exp\left(-\frac{Q_{di}}{RT}\right) \left(\frac{t}{\tau}\right)^{\frac{1-m_i}{m_i}}, \qquad \text{with } i = \{\alpha;\beta\}. \tag{19}$$

where K_i is a constant, Q_{di} is an activation energy, m is the temporal exponent and τ is a characteristic time. In this application τ is set to 10s since it is the characteristic time of a reactivity initiated accident. 16 parameters have finally to be identified in Equations (18) and (19).

An initial set of parameters is identified using Equations (15) and (16) and an assumption of a serial distribution of the phases. Not enough data on the microstructure evolution are available in the literature. It follows that the uniqueness of the solution is not ensured. To obtain physically acceptable results the initial grain size was constraint to be inferior than 10 μm and the maximal grain size at 100s was bounded to be inferior than 50μm. These boundaries were set following the microstructure data of [30] for Zircaloy-4 and of [33] for M5 alloy). The idea here is to show that a grain growth contribution in the creep law enables well reproducing the hardening of the material. Additional data on the microstructure evolution would be necessary to obtain the true evolution of the grain size during the experiments.

The evolution of the objective function is given in Figure 10. In this case the initial error is high because the ballooning deformation of the sample generates a complex stress state within the sample, which therefore cannot be well approximated by the Equation (15). The residual decreases quickly in four iterations up to a converged value equal to 2.7 times the noise level. The values of the parameters of Equations (18) and (19) are given in Table 6.

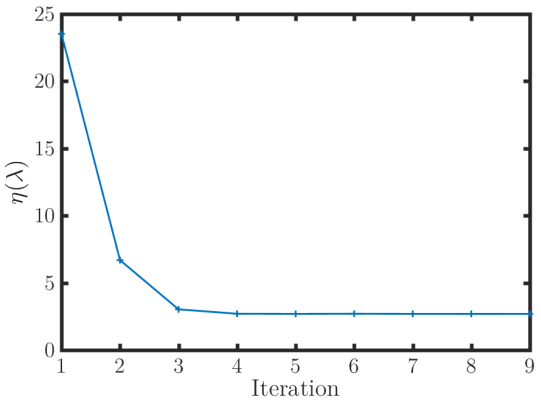

Figure 10: Evolution of the residual η for the identification of a creep law with a grain size contribution reproducing the first 100 seconds of eight experiments performed in the two-phase domain.

The evolution of the grain size for the α and β phase is given in Figure 11 for a test performed at 930 °C. The α grain size does not evolve significantly with time while the β grains grow from very small grain size (nucleation) to several tens of microns. These results are consistent with the results of the literature [30, 33]. Figure 12 compares the radial displacement normalized by the initial inner radius obtained experimentally and numerically at the center of the ROI. The grain size contribution enables the secondary stage of creep to be well reproduced with mean error on the radial displacement rates of 6.6%. Adding a grain growth contribution in the creep law seems then to be a good way of reproducing the hardening of the material in the two-phase domain. Other sources could also be responsible of the non-linear hardening observed during the tests, such as a microstructure evolution of the material or a strain hardening mechanism. This may be investigated in further studies.

	$\ln(A_i)$	n_i	Q_i (kJ.mol^{-1})	g_i	K_i	Q_{di} (kJ.mol^{-1})	m_i	D_{0i} (μm)
$i=\alpha$	35.5	1.31	411.5	3.5	0.38	26.4	1.0	5.0
$i=\beta$	24.2	3.47	371.1	1.0	62.37	50.1	4.0	1.47

Table 6: Values of the parameters of Equations (18) and (19) with $i=\{\alpha;\beta\}$.

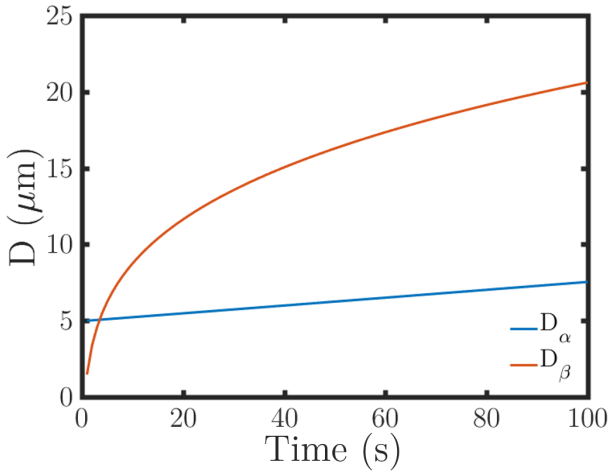

Figure 11: Evolution of the α and the β grain sizes obtained for a temperature of 930 °C using the Equation (19) and the set of parameters given in Table 6.

5. Summary and Conclusion

In this work, a creep model weakly coupled to the phase transformation of the material has been identified for Zircaloy-4 fuel claddings in simulated post-DNB conditions, based on the results of [6]. This model, being the very first identified in such conditions, is expected to be a very good start in the study of the creep response of zirconium alloys under very high heating rate. The temperatures of interest in this work range from 840 to 1020 °C, the heating rate is about 1200 °C/s, and the stress level ranges from around 5 to 8 MPa. The identified model reproduces the first 10 seconds of the experiments with a mean error on the radial displacement rates of around 10%. It was shown that the heating rate seems to have no impact on the activated creep mechanisms. A diffusion creep is identified in the α phase and a dislocation creep is identified in the β phase. These creep mechanisms are consistent with the grain sizes characterized in [6] on the *post-mortem* samples. On the contrary, the activation energies identified in simulated post-DNB conditions are much higher than the usual values found in LOCA conditions. Additional microstructure analysis should be carried out to better understand the underlying mechanisms of such a difference. The model of this work is currently being implemented in the SCANAIR software developed by the French Institute for Radiological Protection and Nuclear Safety (IRSN), which simulates a reactivity initiated accident [34, 35].

An extension of the creep law to the first 100 seconds has also been proposed for 8 experiments performed in the two-phase domain to reproduce the non linearity of the creep response at higher time scale. This extension is based on adding the grain growth contribution in the Norton's law. The identification led to a very good agreement between experimental and numerical results with mean error on the radial displacement rates of around 7%. Although there is a lack of data about the grain size evolution to ensure the uniqueness of the parameter values, these results are expected to be of great interest for the zirconium community in the nuclear industry.

From a numerical point of view, an identification procedure has been proposed to identify a constitutive model based on experiments carried out on tubular samples, where the loading conditions are solely known in the region seen by the cameras. Only the ROI was modeled to reproduce the experiments. The boundary conditions are imposed using the displacements measured by stereo-correlation, and a Love-Kirchhoff kinematic was imposed to constraint the external section of the ROI. The method was first validated on a virtual test case representative of the real experiments before being applied to the true one. The sensitivity of the calculations to the creep parameters was also presented to ensure a fast convergence of the algorithm and minimize the risk of finding a local solution.

Acknowledgments

The authors acknowledge with thanks financial support of this work from EdF and Institut Carnot Ingénierie@Lyon. The authors want also to express their thanks to J. Réthoré for the useful discussions about inverse problems and to ATYS Consulting Group for helping on the induction problematic.

References

[1] V. Bessiron, Modelling of clad-to-coolant heat transfer for RIA applications, Journal of Nuclear Science and Technology 44 (2) (2007) 211–221. doi:10.1080/18811248.2007.9711275.

[2] D. A. Porter, K. E. Easterling, M. Sherif, Phase transformations in metals and alloys, CRC press, 2009.

[3] T. Forgeron, J. C. Brachet, F. Barcelo, A. Castaing, J. Hivroz, J. P. Mardon, C. Bernaudat, Experiment and Modeling of Advanced Fuel Rod Cladding Behavior Under LOCA Conditions: Alpha-Beta Phase Transformation Kinetics and EDGAR Methodology, in: Zirconium in the Nuclear Industry: Twelfth International Symposium, 2000, pp. 256–278. doi:10.1520/STP14303S.

[4] T. Jailin, N. Tardif, J. Desquines, M. Coret, M. Baietto, V. Georgenthum, Experimental study and modelling of the phase transformation of Zircaloy-4 alloy under high thermal transients, Materials Characterization 162. doi:10.1016/j.matchar.2020.110199.

[5] T. Jailin, N. Tardif, J. Desquines, M. Coret, M.-C. Baietto, T. Breville, P. Chaudet, V. Georgenthum, Mechanical behavior of as-fabricated Zircaloy-4 claddings under the simulated thermo-mechanical post-DNB conditions of a Reactivity Initiated Accident (RIA), in: TopFuel, Prague, 2018.
URL https://hal.archives-ouvertes.fr/hal-01863256/document

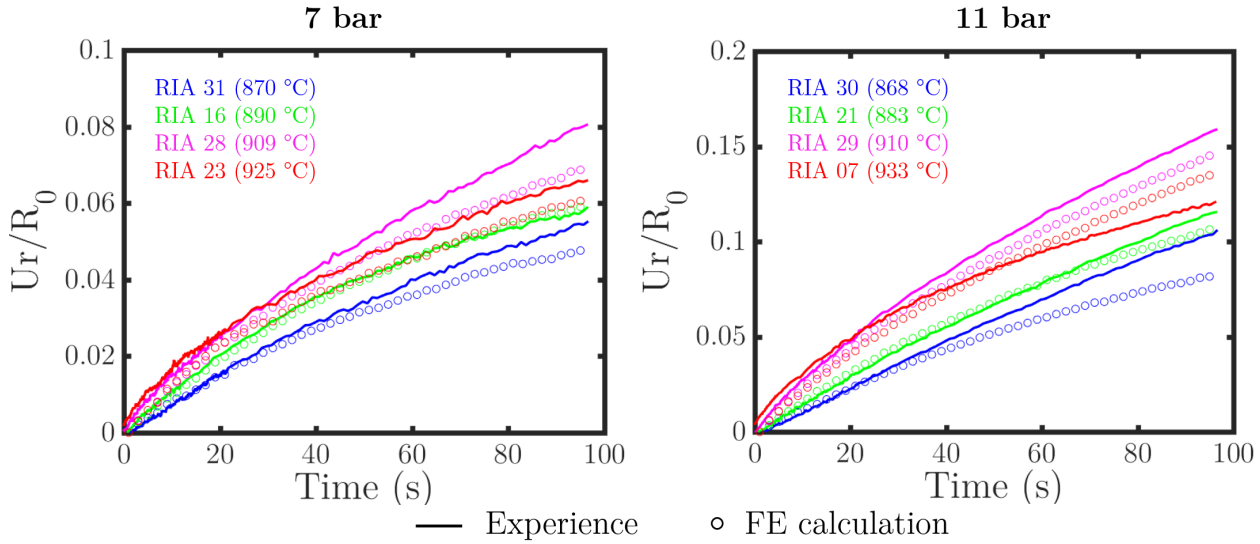

Figure 12: Comparison of the radial displacement evolution at the center of the ROI between experimental to numerical results.

[6] T. Jailin, N. Tardif, J. Desquines, P. Chaudet, M. Coret, M.-C. Baietto, V. Georgenthum, Thermo-mechanical behavior of Zircaloy-4 claddings under simulated post-DNB conditions, Journal of Nuclear Materials 531. doi:10.1016/j.jnucmat.2020.151984.

[7] T. Torimaru, T. Yasuda, M. Nakatsuka, Changes in mechanical properties of irradiated Zircaloy-2 fuel cladding due to short term annealing, Journal of Nuclear Materials 238 (2-3) (1996) 169–174. doi:10.1016/S0022-3115(96)00451-5.

[8] J. Ribis, F. Onimus, J. Béchade, S. Doriot, A. Barbu, C. Cappelaere, C. Lemaignan, Experimental study and numerical modelling of the irradiation damage recovery in zirconium alloys, Journal of Nuclear Materials 403 (1-3) (2010) 135–146. doi:10.1016/j.jnucmat.2010.06.012. URL http://dx.doi.org/10.1016/j.jnucmat.2010.06.012

[9] S. Banerjee, P. Mukhopadhyay, Phase Transformations: Examples from Titanium and Zirconium Alloys, Elsevier, 2010.

[10] C.-t. Nguyen, Microstructure Changes during Fast β Cycles of Zirconium Alloys, Ph.D. thesis, University of Manchester (2017).

[11] K. T. Kavanagh, R. W. Clough, Finite element applications in the characterization of elastic solids, International Journal of Solids and Structures 7 (1) (1971) 11–23. doi:10.1016/0020-7683(71)90015-1. URL http://dx.doi.org/10.1016/0020-7683(71)90015-1

[12] J. Réthoré, Muhibullah, T. Elguedj, M. Coret, P. Chaudet, A. Combescure, Robust identification of elasto-plastic constitutive law parameters from digital images using 3D kinematics, International Journal of Solids and Structures 50 (1) (2013) 73–85. doi:10.1016/j.ijsolstr.2012.09.002.

[13] F. Mathieu, H. Leclerc, F. Hild, S. Roux, Estimation of Elastoplastic Parameters via Weighted FEMU and Integrated-DIC, Experimental Mechanics 55 (1) (2015) 105–119. doi:10.1007/s11340-014-9888-9.

[14] T. Pottier, F. Toussaint, P. Vacher, Contribution of heterogeneous strain field measurements and boundary conditions modelling in inverse identification of material parameters, European Journal of Mechanics / A Solids 30 (3) (2011) 373–382. doi:10.1016/j.euromechsol.2010.10.001. URL http://dx.doi.org/10.1016/j.euromechsol.2010.10.001

[15] D. Campello, N. Tardif, J. Desquines, M. C. Baietto, M. Coret, A. Maynadier, P. Chaudet, Validation of a multimodal set-up for the study of zirconium alloys claddings' behaviour under simulated LOCA conditions, Strain 54 (5) (2018) 1–14. doi:10.1111/str.12279.

[16] T. Jailin, N. Tardif, J. Desquines, M. Coret, M.-C. Baietto, T. Breville, P. Chaudet, V. Georgenthum, Coupled NIRT / 3D-DIC for a FEMU Identification of the Thermo-Mechanical Behavior of Zr-4 Claddings Under Simulated Reactivity Initiated Accident, in: Residual Stress, Thermomechanics & Infrared Imaging and Inverse Problems, Vol. 6, Springer, Cham, Reno, 2020, Ch. 7, pp. 41–47. doi:10.1007/978-3-030-30098-2_7.

[17] J.-B. Leblond, J. Devaux, A new kinetic model for anisothermal metallurgical transformations in steels including effect of austenite grain size, Acta Metallurgica 32 (1) (1984) 137–146. doi:10.1016/0001-6160(84)90211-6.

[18] D. L. Hagrman, G. A. Reymann, MATPRO-Version 11: A handbook of materials properties for use in the analysis of light water reactor fuel rod behavior, Tech. rep., Idaho National Engineering Lab., Idaho Falls (USA) (1979). doi:10.2172/6442256.

[19] J. Lemaitre, J. L. Chaboche, Mechanics of solid materials, Cambridge university press, 1994.

[20] D. Campello, N. Tardif, M. Moula, M. C. Baietto, M. Coret, J. Desquines, Identification of the steady-state creep behavior of Zircaloy-4 claddings under simulated Loss-Of-Coolant Accident conditions based on a coupled experimental/numerical approach, International Journal of Solids and Structures 115-116 (2017) 190–199. doi:10.1016/j.ijsolstr.2017.03.016.

[21] D. Kaddour, S. Frechinet, A. F. Gourgues, J. C. Brachet, L. Portier, A. Pineau, Experimental determination of creep properties of zirconium alloys together with phase transformation, Scripta Materialia 51 (6) (2004) 515–519. doi:10.1016/j.scriptamat.2004.05.046.

[22] M. E. Kassner, Fundamentals of Creep in Materials, Butterworth-Heinemann, 2015. doi:10.1016/B978-0-08-099427-7.00001-3.

[23] T. A. Hayes, M. E. Kassner, Creep of Zirconium and Zirconium Alloys, in: Mechanical and Creep Behavior of Advanced Materials, Springer, Cham, 2017, pp. 103–114. doi:10.1007/978-3-319-51097-2_9.

[24] J. Qu, M. Cherkaoui, Fundamentals of micromechanics of solids, Wiley Hoboken, 2006. doi:10.1002/9780470117835.

[25] J. W. C. Dunlop, Y. J. M. Bréchet, L. Legras, H. S. Zurob, Modelling isothermal and non-isothermal recrystallisation kinetics: Application to Zircaloy-4, Journal of Nuclear Materials 366 (1-2) (2007) 178–186. doi:10.1016/j.jnucmat.2006.12.074.

[26] J. C. Simo, M. Rifai, A class of mixed assumed strain methods and the method of incompatible modes, International journal for numerical methods in engineering 29 (8) (1990) 1595–1638. doi:10.1002/nme.1620290802.

[27] A. T. Donaldson, R. C. Ecob, A transition stress in the creep of an alpha phase zirconium alloy at high temperature, Scripta metallurgica 19 (11) (1985) 1313–1318.

[28] C. E. L. Hunt, D. E. Foote, High temperature strain behavior of Zircaloy-4 and Zr-2.5 Nb fuel sheaths, in: Zirconium in the Nuclear Industry, ASTM International, 1977, pp. 50–65. doi:10.1520/STP35564S.

[29] H. E. Rosinger, P. C. Bera, W. R. Clendening, Steady-state creep of zircaloy-4 fuel cladding from 940 to 1873 k, Journal of Nuclear materials 82 (2) (1979) 286–297. doi:10.1016/0022-3115(79)90011-4.

[30] H. E. Sills, R. A. Holt, Predicting high-temperature transient deformation from microstructural models, in: Zirconium in the Nuclear Industry, ASTM International, 1979. doi:10.1520/STP36688S.

[31] Y. S. Lee, D. W. Kim, D. Y. Lee, W. S. Ryu, Effect of Grain Size on Creep Properties of Type 316LN Stainless Steel, Metals and Materials International 7 (2) (2001) 107–114. doi:10.1007/BF03026948.

[32] D. L. Douglass, The Metallurgy of Zirconium, IAEA, 1971.

[33] G. Trégo, J. Brachet, V. Vandenberghe, L. Portier, L. Gélébart, R. Chosson, J. Soulacroix, S. Forest, A.-F. Gourgues-Lorenzon, Influence of grain size on the high-temperature creep behaviour of M5 Framatome zirconium alloy under vacuum, Journal of Nuclear Materialsdoi:10.1016/j.jnucmat.2021.153503.

[34] A. Moal, V. Georgenthum, O. Marchand, SCANAIR: A transient fuel performance code. Part One: General modelling description, Nuclear Engineering and Design 280 (2014) 150–171. doi:10.1016/j.nucengdes.2014.03.055.

[35] V. Georgenthum, A. Moal, O. Marchand, SCANAIR a transient fuel performance code. Part two: Assessment of modelling capabilities, Nuclear Engineering and Design 280 (2014) 172–180. doi:10.1016/j.nucengdes.2014.04.030.